

# Physics-augmented Deep Learning with Adversarial Domain Adaptation: Applications to STM Image Denoising

Jianxin Xie\*, Wonhee Ko, Rui-Xing Zhang, Bing Yao

**Abstract**—Image denoising is a critical task in various scientific fields such as medical imaging and material characterization, where the accurate recovery of underlying structures from noisy data is essential. Although supervised denoising techniques have achieved significant advancements, they typically require large datasets of paired clean-noisy images for training. Unsupervised methods, while not reliant on paired data, typically necessitate a set of unpaired clean images for training, which are not always accessible. In this paper, we propose a physics-augmented deep learning with adversarial domain adaption (PDA-Net) framework for unsupervised image denoising, with applications to denoise real-world scanning tunneling microscopy (STM) images. The underlying physics model is first used to generate simulation data and envision the ground truth for denoised STM images. Additionally, built upon Generative Adversarial Networks (GANs), we incorporate a cycle-consistency module and a domain adversarial module into our PDA-Net to address the challenge of lacking paired training data and achieve information transfer between the simulated and real experimental domains. Finally, we propose to implement feature alignment and weight-sharing techniques to fully exploit the similarity between simulated and real experimental images, thereby enhancing the denoising performance in both the simulation and experimental domains. Experimental results demonstrate that the proposed PDA-Net successfully enhances the quality of STM images, offering promising applications to enhance scientific discovery and accelerate experimental quantum material research.

**Note to Practitioners**—This study is motivated by the challenges of denoising images in scientific fields where acquiring clean ground truth data is infeasible. In material characterization (e.g., STM imaging), evaluating denoising performance is difficult because real experimental images inherently contain noise, and their clean counterparts are unavailable. Fortunately, physics-based simulations can generate an unlimited number of clean STM images, offering a valuable resource for guiding the denoising process. This paper presents PDA-Net, a physics-augmented deep learning model designed to enhance the denoising of real-world STM images by leveraging simulation data. By integrating adversarial domain adaptation and cycle-consistency modules, PDA-Net effectively transfers knowledge from simulated to experimental domains, enabling improved denoising performance without requiring clean experimental data.

**Index Terms**—Image Denoising, Domain Adaptation, Unsupervised learning, Adversarial Neural Network, Scanning Tunneling Microscopy

Jianxin Xie (\*corresponding author: hcf7fd@virginia.edu) is with the School of Data Science, University of Virginia, Charlottesville, VA 22904 USA. Wonhee Ko and Rui-Xing Zhang are from the Department of Physics, University of Tennessee at Knoxville. Bing Yao (byao3@utk.edu) is with the Department of Industrial and Systems Engineering, University of Tennessee at Knoxville.

## I. INTRODUCTION

Digital imaging techniques have become indispensable across a range of fields, from medical diagnostics and remote sensing to everyday photography. For example, in the medical field, Magnetic Resonance Imaging (MRI) stands as a vital non-invasive tool, providing detailed images of soft tissues, organs, and other internal structures [1]. The quality of these images is crucial for accurate disease diagnosis and treatment planning [2], [3]. However, the presence of noise, especially in low-field MRI or fast imaging protocols, can significantly compromise image clarity, potentially affecting clinical outcomes. Advanced imaging techniques also play a critical role in scientific research. Scanning Tunneling Microscopy (STM), for example, is a powerful method for examining the local electronic structure of quantum materials at atomic resolution [4]. By leveraging quantitative spectroscopy based on tunneling current, STM enables the visualization of both the geometric and electronic properties of a material's surface. However, STM is highly sensitive to the distance between the tip and sample, making it susceptible to noise that can obscure crucial details and hinder precise analysis [5]. To effectively address this challenge, effective image-denoising models are needed to enhance the image quality for better visualization of materials at the atomic or molecular scale.

Image denoising is a critical preprocessing step in image-based analytics, aimed at removing noise while preserving important image details, such as edges and textures. Recently, deep learning, particularly convolutional neural networks (CNNs) [6], has revolutionized the field of image denoising by leveraging large datasets and designing sophisticated architectures. Despite these advancements, image denoising remains a challenging problem. Many denoising models require a substantial amount of paired training data, i.e., clear and blurred pairs, to learn a trustworthy model. Collecting such paired data in real-world settings can be highly challenging. To cope with this limitation, unsupervised image-denoising approaches via Generative Adversarial Networks (GANs) have been increasingly developed such as CycleGAN [7], DualGAN [8], Pix2pix [9], and UNIT [10]. These methods leverage unpaired data to learn mappings between different image domains, achieving unsupervised image denoising. Nevertheless, traditional unsupervised denoising models assume the availability of both noisy and clear images for training. It is important to note that, in many real-world scenarios such as STM, the acquisition of noise-free images is impractical due

to the extreme sensitivity to environmental vibrations, thermal drift, electronic noise, and inherent equipment limitations [11]. This lack of clear images presents a significant challenge for existing models in denoising STM images.

In this work, we propose a novel physics-augmented adversarial domain adaptive model (PDA-Net) to achieve effective denoising of experimental STM images despite the absence of real-world clear images. Specifically, our contributions are summarized as follows:

(1) We leverage the physical laws governing electron scattering within materials to generate a large volume of unpaired simulated clear and blurry STM images. The simulated image pairs provide essential clean and noisy feature information as a foundation to construct the denoising model for real-world experimental image denoising.

(2) The novel design of our PDA-Net features with the combination of a cycle-consistency and a domain adversarial module. The cycle-consistency module is proposed to address the challenge of lacking paired training data and ensure the preservation of original image patterns in the denoised outputs. The domain adversarial module is proposed to facilitate simulation-to-real domain adaptation, enabling effective denoising of experimental images using knowledge extracted from simulated images.

(3) To fully exploit the high similarity between simulated and real experimental images, we propose to implement feature alignment and weight sharing between the two denoising networks for simulated and experimental images, thereby enhancing the denoising performance in both the simulation and experimental domains.

This effective STM denoising method holds great significance because it will enhance the clarity and accuracy of the atomic-scale structures observed, which is crucial for advancing scientific understanding of material properties, atomic arrangements, and surface phenomena, facilitating new physics discovery in nanotechnology and materials science. The remainder of this paper is organized as follows: Section 2 presents the literature review of image denoising. Section 3 introduces the proposed PDA-Net framework. Section 4 shows the numerical experiments of the proposed PDA-Net method to denoise the simulated blurry images and lab-collected STM images. Section 5 concludes the present investigation.

## II. LITERATURE REVIEW

### A. Image denoising models

Traditional statistical models for image denoising include spatial domain methods and transform domain methods [12]. Spatial domain methods operate directly on the pixel values of the image to reduce noise while preserving important features [13], [14], which have been widely used due to their simplicity and high efficiency in various noise conditions. However, it has been recognized that spatial domain methods have disadvantages in potentially blurring fine details and edges along with noise, leading to a loss of important image information. Transform domain methods were then introduced to better separate noises from signals, leveraging the frequency domain representation of images [15]–[17]. These methods

suppress certain frequency components of the raw image that may represent noise. Denoising is then achieved by reconstructing the image from the modified frequency domain using the inverse transform, thereby preserving structural details while reducing noise. However, these traditional denoising methods heavily rely on pre-defined mathematical models and assumptions about noise and signal, lacking the flexibility to adapt to varying noise patterns and image structures.

To meet the growing demand for high-quality images, researchers have engaged deep learning as a powerful alternative. In particular, CNNs have emerged as the most commonly used network architecture to learn complex patterns directly from data [18], [19], enabling blind image denoising, where no prior knowledge of the blurring function is known [20]–[23]. Based on CNN backbone, various enhancements, such as perceptual loss [24]–[26], attention mechanism [27], [28], multi-scale learning [29]–[31], and vision transformer [32]–[34], have been proposed and validated to be effective in improving the denoising performance. Yet, most denoising models require a substantial amount of paired training data (i.e., clear and blurred pair), which are challenging to acquire in real-world scenarios, to learn a trustworthy model.

Recently, GAN-based models [35] have emerged as a powerful approach for image denoising, offering significant improvements over traditional deep learning methods. GANs consist of two neural networks, a generator and a discriminator, that are trained simultaneously through adversarial learning. The generator tries to create realistic data and the discriminator attempts to distinguish between real and generated data. The unique structure of GANs, where the discriminator oversees the images created by the generator, ensures that the generated images possess the expected attributes, i.e., denoised features in this study. This adversarial architecture makes GANs highly suitable for unsupervised image denoising, as they can learn from unpaired data and produce high-quality denoised images without requiring extensive noisy-clear paired datasets.

A notable example is the CycleGAN framework [7], which employs cycle-consistency loss to ensure that the mapping between noisy and clean image domains is robust, even without paired datasets. Multiple effective denoising approaches have been built upon CycleGAN, demonstrating its effectiveness in producing high-quality denoised images. For example, Lu et al. [25] proposed a disentangled framework to split the content and the blur features of blurred images. They engaged the cycle-consistency model to match the content structures of restored images with the original ones. Zhao et al. [36] proposed a lightweight unsupervised image deblurring framework with a parameter-free domain contrastive unit to realize more efficient training and inference while preserving the denoising quality. Kwon [37] et al. engaged one invertible generator to fulfill the cycle consistency condition instead of two generators, hence increasing the training efficiency. However, unsupervised denoising models in the literature are based on the sense that, although clear and noisy images are not paired, clear images are widely accessible. They did not consider the scenarios where real-world clear images are not available. Even though some work [38] employs iterative

reconstruction algorithms to create clear image benchmarks, this method imposes high computational costs and has a unique limitation of requiring a properly designed prior that accurately captures the characteristics of input images [39].

### B. Domain Adaptation

Domain adaptation [40], a transfer learning technique, has been increasingly investigated for addressing domain shift and bias, particularly in scenarios with limited or no labeled data. This method enables the distinguish of domain-specific characteristics and the generation of complex samples across diverse domains. For example, Liu et al. [41] proposed coupled GANs to learn a joint distribution of multi-domain images, facilitating the generation of samples across different domains. Notably, in the work by Tzeng et al. [42], the authors proposed the adversarial discriminative domain adaptation model, which utilizes an untied generative mapping to produce output and discriminators to align representations from the source and target domains through adversarial training. Following these pioneering works, many subsequent domain adaptation methods have been proposed with enhanced performance and broader applicability. For instance, the CyCADA model by Hoffman et al. [43] introduced a cycle-consistent adversarial approach to adapt representations at both pixel and feature levels, significantly improving the transferability across domains. Lee et al. [44] proposed a content-adaptive domain transfer module, which disentangles image representations into content and style, preserving content structure while effectively transferring style, thereby achieving high-quality domain transfer images.

Due to the high quality of feature learning across domains, domain adaptation is also proving to be highly effective in the field of image denoising. For example, Lin et al. [45] used domain adaptation to map a source noisy image to a target noisy image, both sharing the same ground truth noise-free image, thereby expanding the training set. Li et al. [46] pretrained a modularized adaptive processing neural network, which itself serves as a denoising model, to preprocess training images using paired datasets from multiple domains, thereby enforcing domain adaptation and generating content features with combined knowledge from different domains. Deng et al. [47] designed a disentanglement-reconstruction network to interchange the noisy pattern and image content between images from two domains. The new images then pass through a denoising generator and are encouraged to match the original paired clear images. However, most existing domain adaptive denoising models either engage the domain adaptation during the preprocessing phase, which still requires clear images to prepare the training inputs, or paired noisy-clean images are demanded to constrain the domain adaptive denoising generator. To the best of our knowledge, we are the first to create an unsupervised domain adaptive denoising model that addresses the scenario where no clear image is available for the target denoising domain.

## III. RESEARCH METHODOLOGY

We propose a PDA-Net for imaging denoising in an unsupervised manner by leveraging physics-based simulation

and novel design of network architectures. Fig. 1 shows the overall flowchart of our PDA-Net model. Here, we use  $I_S$  to denote the simulated clean images generated from the physics-based model,  $I_{BS}$  to denote the simulated blurry images, and  $I_E$  to denote the experimental images. Our goal is to learn a simulation-denoising model  $G_D$  that can generate high-quality deblurred simulated images  $I_{BS}^D$  from  $I_{BS}$ , i.e.,  $I_{BS}^D = G_D(I_{BS})$ , which will be further leveraged to construct an experimental-denoising model  $G_{DA}$  that generates high-quality deblurred experimental images  $I_E^{DA}$  from  $I_E$ , i.e.,  $I_E^{DA} = G_{DA}(I_E)$ . Each component in the flowchart (i.e., Fig. 1) is described in detail in the following subsections.

### A. Adversarial Denoising Model for Physics-based Simulation Images

The simulation denoising model, characterized by a denoising generator  $G_D$ , aims to sharpen the simulated blurry images  $I_{BS}$ . To facilitate unsupervised learning and ensure the generated images from  $G_D$  look similar to the simulated clear images  $I_S$ , we introduce an adversarial discriminator,  $D_D$ , hoping the produced deblurred sample  $I_{BS}^D$  by  $G_D$  can fool  $D_D$ . Specifically,  $D_D$  aims to differentiate the generated deblurred images  $I_{BS}^D$  from the simulated clear images  $I_S$ , forcing the generator  $G_D$  to increasingly generate accurate and realistic deblurred images. This goal is achieved by optimizing the following adversarial objective function:

$$\min_{G_D} \max_{D_D} \mathcal{L}_{D_D} = \mathbb{E}_{I_S \sim p(I_S)} [\log D_D(I_S)] + \mathbb{E}_{I_{BS} \sim p(I_{BS})} [\log(1 - D_D(G_D(I_{BS})))] \quad (1)$$

In this adversarial game, the generator  $G_D$  and discriminator  $D_D$  are trained such that  $G_D$  seeks to minimize this adversarial loss, while  $D_D$  tries to maximize it. This min-max training enables  $G_D$  to produce deblurred images  $I_{BS}^D$  that are increasingly indistinguishable from the simulated clear image  $I_S$ , while simultaneously enhancing  $D_D$ 's ability to discern  $I_S$  from the generated ones. It is worth noting that the neural network is trained in an unsupervised manner, meaning there is no direct one-to-one correspondence between the clear image  $I_S$  and its blurred counterpart  $I_{BS}$  in the training set.

### B. Cycle Consistency-enhanced Denoising of Physics-based Simulation Images

Because no pairwise supervision is provided, the sole unsupervised adversarial denoising model often suffers from instability issue, generating non-ideal deblurred results. This is because, while the adversarial loss in Eq. (1) encourages the generated deblurred sample  $I_{BS}^D$  to resemble the distribution of the clear image  $I_S$  simulated by the physics-based model, there is no assurance that  $I_{BS}^D$  will maintain the structure or pattern of the original input  $I_{BS}$  of the denoising generator  $G_D$  [43]. To cope with the limitation and ensure the generated deblurred images preserve the patterns of the original inputs, a cycle consistency constraint [7], [48], [49] is imposed on the generating process. The cycle-consistency constraint is achieved through the following two mechanisms:

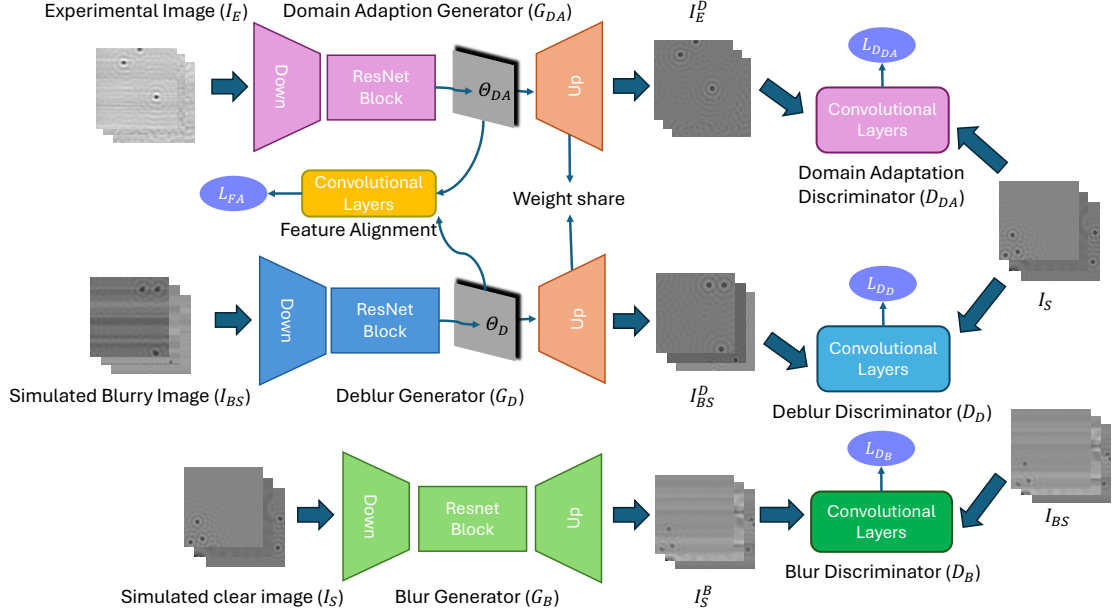


Fig. 1: Overview of the PDA-Net model. The PDA-Net model engages three generators.  $G_D$  aims to denoise the simulated blurry image  $I_{BS}$ .  $G_B$ , on the contrary, is set to create blurry images from the simulated clear images  $I_S$ .  $G_{DA}$  is a domain adaptive generator that is specialized to denoise the real-world images  $I_E$ . The purpose of auxiliary blur generator and discriminator, i.e.,  $G_B$  and  $D_B$  is to formulate a cycle-consistency regularization (see Fig. 2) and further assist the learning of  $G_D$ .  $D_D$  and  $D_{DA}$  are set to discriminate the deblurred images  $I_{BS}^D$  and  $I_E^D$  with the clear images.

1) *Adversarial training in the blurred simulated image domain:* The goal here is to learn a blurring generator  $G_B$  that can create blurry images from the simulated clear images  $I_S$ , i.e.,  $I_S^B = G_B(I_S)$ . Similar to the adversarial model described in III-A, a discriminator  $D_B$  is deployed to classify the blurry image  $I_{BS}$  provided by the physics-based simulation from generated ones  $I_S^B$ . The adversarial objective function can be written as:

$$\min_{G_B} \max_{D_B} \mathcal{L}_{D_B} = \mathbb{E}_{I_{BS} \sim p(I_{BS})} [\log D_B(I_{BS})] + \mathbb{E}_{I_S \sim p(I_S)} [\log(1 - D_B(G_B(I_S)))] \quad (2)$$

Optimizing Eq. (2) enables  $G_B$  to generate blurred images  $I_S^B$  that are increasingly indistinguishable from the blurred image  $I_{BS}$  simulated by the physics-based model, while simultaneously refining  $D_B$ 's ability to discern  $I_{BS}$  from  $I_S^B$ .

2) *Cycle-Consistency Loss:* To further enforce the cycle consistency constraint, we need to ensure that the deblurred image  $I_{BS}^D$  generated by denoising generator  $G_D$  can be reblurred to replicate the original blurred samples, and meanwhile the blurred image  $I_S^B$  generated by the blurring generator  $G_B$  can be deblurred and converted back to clear images. Hence, we can define a forward translation from generated deblurred images to blurred images as:

$$\hat{I}_{BS} = G_B(I_{BS}^D)$$

where we expect  $\hat{I}_{BS} \approx I_{BS}$ . A backward translation from generated blurred images to deblurred images is defined as:

$$\hat{I}_S = G_D(I_S^B)$$

where the cycle should bring the generated blurred images  $I_S^B$  back to their clear version, i.e.,  $\hat{I}_S \approx I_S$ . The cycle consistency loss is defined as the L1 regularization on the reconstruction errors of both translations:

$$\mathcal{L}_{cyc} = \mathcal{L}_{cyc}^f + \mathcal{L}_{cyc}^b \quad (3)$$

where  $\mathcal{L}_{cyc}^f = \mathbb{E}_{I_{BS} \sim p(I_{BS})} [\|I_{BS} - \hat{I}_{BS}\|_1]$   
 $\mathcal{L}_{cyc}^b = \mathbb{E}_{I_S \sim p(I_S)} [\|I_S - \hat{I}_S\|_1]$

Minimizing the cycle-consistency loss will further narrow down the distribution of the generated images and preserve the patterns of original images, leading to enhanced performance in imaging denoising in the simulation domain.

### C. Simulation-to-Real Domain Adaption for Experimental Image Denoising

The simulation-denoising model  $G_D$  is expected to provide good denoising performance for simulated images, leveraging the advantages of adversarial objectives and the cycle-consistency constraint. However, directly applying  $G_D$ , trained on simulated images, to denoise real experimental images, denoted as  $I_E$ , is inappropriate and may generate suboptimal results due to the domain shift issue. Training an experimental-denoising model from scratch using real-world experimental images is generally infeasible because it is extremely difficult or expensive to collect noise-free experimental images. To cope with this challenge, this subsection introduces a Simulation-to-Real Domain Adaption method to adapt the simulation-denoising model  $G_D$  such that it performs well on denoising real-world experimental data without any additional supervision from noise-free experimental images.

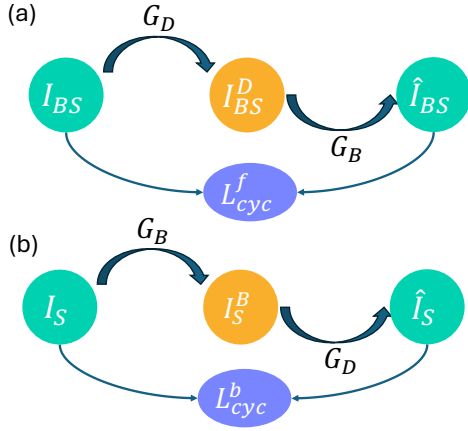


Fig. 2: Given the intuition that translating images from one domain to another and then reversing the process should restore the original images, the cycle is expected to return the generated images to their original state, we design (a) a forward consistency translate with loss  $\mathcal{L}_{cyc}^f$  and (b) a backward consistency translate with loss  $\mathcal{L}_{cyc}^b$ .

For implementing the domain adaptation, we first create a base generator  $G_{DA}$ , which inherits the same neural network structure with  $G_D$ . However, the neural network parameters in  $G_{DA}$  used for deblurring real-world images  $I_E$  will differ from those in  $G_D$  due to the unavoidable domain shift between the simulation and real experimental domains. Thus, it is necessary to retrain  $G_{DA}$  and fine-tune the neural network parameters specifically for the experimental image domain to ensure effective performance. Here, we propose to achieve domain adaptation and optimize  $G_{DA}$  in an adversarial manner by incorporating a domain discriminator  $D_{DA}$ . Specifically,  $D_{DA}$  evaluates the deblurred experimental images, denoted as  $I_E^D = G_{DA}(I_E)$ , and compares them against the clear simulated images  $I_S$  by continuously challenging  $G_{DA}$  to produce deblurred outputs whose sharpness degree closely resembles that in  $I_S$ . The adversarial domain-adaptation objective function is defined as:

$$\min_{G_{DA}} \max_{D_{DA}} \mathcal{L}_{D_{DA}} = \mathbb{E}_{I_S \sim p(I_S)} [\log D_{DA}(I_S)] + \mathbb{E}_{I_E \sim p(I_E)} [\log(1 - D_{DA}(G_{DA}(I_E)))] \quad (4)$$

The proposed domain adaption technique aims to eliminate the domain discrepancy between the simulated and real experimental images such that the denoising process learned from simulated images can be readily applicable to denoising the real-world experimental images. However, using a separate adversarial generator  $G_{DA}$  for our target domain, i.e., experimental imaging, without any connection to the simulation domain, may require a larger amount of data from both domains and a longer training time to achieve good performance, as it must independently learn all necessary features from the ground up. Additionally, isolating  $G_{DA}$  from  $G_D$  gives up the opportunity to utilize valuable, domain-invariant features learned from the simulation domain, potentially reducing the effectiveness of  $G_{DA}$  in denoising images from the real experimental domain.

Given that both the simulated images, derived using physics laws, and the experimental images depict the same physical subject (e.g., Cu atoms in STM experiments), there should inherently be substantial pattern similarities between the images from the two domains. Such similarities need to be effectively explored and incorporated into the generators  $G_D$  and  $G_{DA}$  to improve the denoising performance of the model. Hence, we propose to leverage the weight sharing and feature alignment mechanisms to enable the two generators to incorporate the similarity information from the simulation and real experimental domains.

1) *Weight sharing*: As depicted in Fig. 1,  $G_D$  and  $G_{DA}$  share the same network structure, i.e., an encoder-decoder architecture with a ResNet block at the bottleneck. We assume that the Down and ResNet Block components within  $G_D$  and  $G_{DA}$  are trained independently, enabling each to learn domain-specific attributes for effectively denoising the respective input images, i.e.,  $I_{BS}$  and  $I_E$ . The weight sharing is then implemented in the Upsampling blocks in  $G_D$  and  $G_{DA}$ , tasking with further purifying the common noisy patterns that appear in both domains and constructing feature maps to the original image resolution. This strategy facilitates the transfer of learned representations from the simulation to the experimental domain, ensuring that both generators benefit from shared knowledge and reduce redundancy in learning. Based on the premise that images from two distinct domains exhibit similar high-level attributes, as they both characterize the same subject (i.e., copper single crystal in our later case study), the upsampling blocks in  $G_D$  and  $G_{DA}$  are configured to share the same weights:

$$\theta_{DA}^{up} = \theta_D^{up} \quad (5)$$

where  $\theta_{DA}^{up}$  and  $\theta_D^{up}$  are the neural network parameters for upsampling blocks (orange) in  $G_D$  and  $G_{DA}$ , respectively.

2) *Feature Alignment*: We further engage feature alignment to synchronize the intermediate features that are capable of characterizing the overall input pattern. The individually trained Down and ResNet blocks in both generators are expected to extract blurring information from their own corresponding domains. This allows each generator to precisely address the unique denoising challenges posed by different noise sources—simulated blurring and real-world noisy experimental images, respectively. Consequently, the intermediate feature maps  $\Theta_D = \phi_{G_D}(I_{BS})$  and  $\Theta_{DA} = \phi_{G_{DA}}(I_E)$  should exhibit considerable resemblance to each other after the initial denoising step posed by the Down and ResNet Blocks  $\phi_{G_{DA}}$  and  $\phi_{G_D}$  from  $G_D$  and  $G_{DA}$ , respectively. As such, we define the following discrimination loss function to achieve feature alignment:

$$\min_{\phi_{G_{DA}}, \phi_{G_D}} \max_{D_{FA}} \mathcal{L}_{FA} = \mathbb{E}_{I_E \sim p(I_E)} [\log D_{FA}(\phi_{G_{DA}}(I_E))] + \mathbb{E}_{I_{BS} \sim p(I_{BS})} [\log(1 - D_{FA}(\phi_{G_D}(I_{BS})))] \quad (6)$$

where  $D_{FA}$  is a domain classifier.

By implementing partial weight sharing in  $G_D$  and  $G_{DA}$ , we facilitate the direct transfer of learned features from the simulated domain to the experimental domain. Additionally,

feature alignment helps ensure that the critical features from both domains are processed in comparable ways, enhancing the model's ability to generalize across different sourced image data. This approach effectively reduces the redundancy in learning similar features separately for each domain, optimizing both the performance and data utilization of the model.

Putting together, the final objective function is the weighted sum of all losses mentioned above:

$$\mathcal{L}_{total} = \lambda_D \mathcal{L}_{D_D} + \lambda_B \mathcal{L}_{D_B} + \lambda_{cyc} \mathcal{L}_{cyc} + \lambda_{DA} \mathcal{L}_{D_{DA}} + \lambda_{FA} \mathcal{L}_{F_A} \quad (7)$$

where  $\lambda_D$ ,  $\lambda_B$ ,  $\lambda_{cyc}$ ,  $\lambda_{DA}$ , and  $\lambda_{FA}$  denote the weights characterizing the contribution of the corresponding loss term, which is selected by empirically fine-tuning. Optimizing Eq. (7) will provide both the simulation-denoising and experimental-denoising models:  $\{G_D^*, G_{DA}^*\} = \arg \min_{\{G_D, G_B, G_{DA}, \phi_{G_D}, \phi_{G_{DA}}\}} \max_{\{D_D, D_B, D_{DA}, D_{FA}\}} \mathcal{L}_{total}$ , where  $\phi_{G_D} \subset G_D$ ,  $\phi_{G_{DA}} \subset G_{DA}$ .

#### D. Training Procedure of the PDA-Net

**Algorithm 1** Training Procedure of the proposed PDA-Net model.

---

**Input:**  $\{I_{BS}\}_{b=1}^{N_b}$ ,  $\{I_S\}_{b=1}^{N_b}$ ,  $\{I_E\}_{b=1}^{N_b}$ ,  $N_b$   
**Output:** Trained denoising models:  $G_D^*$  and  $G_{DA}^*$   
**for**  $n = 1$  to maximum epoch  $N_e$  **do**  
  **for**  $b = 1$  to maximum batch number  $N_b$  **do**  
    Generate a batch of synthetic images  $\{I_E^D\}_b$ ,  $\{I_{BS}^D\}_b$ , and  $\{I_S^B\}_b$  using generators  $G_D$ ,  $G_B$ ,  $G_{DA}$ .  
    Compute the discriminators' losses:  $\mathcal{L}_D = \lambda_D \mathcal{L}_{D_D} + \lambda_B \mathcal{L}_{D_B} + \lambda_{DA} \mathcal{L}_{D_{DA}} + \lambda_{FA} \mathcal{L}_{F_A}$ .  
    Update the discriminator parameters  $\{\mathcal{W}_{D_D}, \mathcal{W}_{D_B}, \mathcal{W}_{D_{DA}}, \mathcal{W}_{D_{FA}}\}$  by descending the gradient of  $-\mathcal{L}_D$ . Meanwhile, the network parameters for all the generators are frozen.  
    Compute the generators' losses and cycle-consistency loss:  $\mathcal{L}_{G+C} = \lambda_D \mathcal{L}_{G_D} + \lambda_B \mathcal{L}_{G_B} + \lambda_{DA} \mathcal{L}_{G_{DA}} + \lambda_{cyc} \mathcal{L}_{cyc} + \lambda_{FA} \mathcal{L}_{F_A}$ .  
    Update the generator parameters  $\{\mathcal{W}_{G_D}, \mathcal{W}_{G_B}, \mathcal{W}_{G_{DA}}, \mathcal{W}_{\phi_{G_D}}, \mathcal{W}_{\phi_{G_{DA}}}\}$  by descending the gradient of  $\mathcal{L}_{G+C}$ . Note that  $\mathcal{W}_{\phi_{G_D}} \subset \mathcal{W}_{G_D}$ ,  $\mathcal{W}_{\phi_{G_{DA}}} \subset \mathcal{W}_{G_{DA}}$ . Meanwhile, the network parameters for all the discriminators are frozen.  
  **end for**  
  **if** converge **then**  
    **break**  
  **end if**  
**end for**  
**return**  $G_D^*$ ,  $G_{DA}^*$ ,  $\mathcal{W} = \{\mathcal{W}_{D_D}, \mathcal{W}_{D_B}, \mathcal{W}_{D_{DA}}, \mathcal{W}_{D_{FA}}, \mathcal{W}_{G_D}, \mathcal{W}_{G_B}, \mathcal{W}_{G_{DA}}\}$

---

Algorithm 1 summarizes the training process for the proposed PDA-Net. For each epoch, and within each training batch, the algorithm generates synthetic denoised and blurry images using a set of generators  $G_D$ ,  $G_B$ ,  $G_{DA}$ . The algorithm

then updates the discriminator parameters by descending the gradient of the discriminator loss  $-\mathcal{L}_D$ , where  $\mathcal{L}_D$  is computed by summing the weighted individual losses of  $\mathcal{L}_{D_D}$ ,  $\mathcal{L}_{D_B}$ ,  $\mathcal{L}_{D_{DA}}$ , and  $\mathcal{L}_{D_{FA}}$ . After updating the discriminators, the parameters of generators are updated by descending the gradient of the combined generator and cycle-consistency loss  $\mathcal{L}_{G+C}$ , which also includes a set of weighted losses ( $\mathcal{L}_{G_D}$ ,  $\mathcal{L}_{G_B}$ ,  $\mathcal{L}_{G_{DA}}$ ,  $\mathcal{L}_{cyc}$ , and  $\mathcal{L}_{F_A}$ ). The generators  $G_D$  and  $G_{DA}$  try to produce clear images that are indistinguishable from simulated clear data  $I_S$ , while  $G_B$  aims to yield blurry images that are similar to the simulated blurry ones  $I_{BS}$ .  $\phi_{G_D}$  and  $\phi_{G_{DA}}$ , the Down and Resnet blocks in  $G_D$  and  $G_{DA}$ , strive to align the intermediate feature maps  $\Theta_D$  and  $\Theta_{DA}$  that are indistinguishable to  $D_{FA}$ . According to the loss functions in Eq. (1), Eq. (2), and Eq. (4), the generator losses are formulated as:

$$\begin{aligned} \mathcal{L}_{G_D} &= \mathbb{E}_{I_{BS} \sim p(I_{BS})} [\log(1 - D_D(G_D(I_{BS})))] \\ \mathcal{L}_{G_B} &= \mathbb{E}_{I_S \sim p(I_S)} [\log(1 - D_B(G_B(I_S)))] \\ \mathcal{L}_{G_{DA}} &= \mathbb{E}_{I_E \sim p(I_E)} [\log(1 - D_{DA}(G_{DA}(I_E)))] \end{aligned} \quad (8)$$

This iterative process continues until convergence. The algorithm then returns the trained network parameters  $\mathcal{W}$  and the two denoising models:  $G_D^*$  and  $G_{DA}^*$ . During the inference, the testing inputs are passed through  $G_D^*$  and  $G_{DA}^*$  to produce a deblurred version of simulated blurry images and real-world experimental images.

## IV. EXPERIMENTAL DESIGN AND RESULTS

In quantum material research, STM has been a powerful experimental probe for delineating electronic structures at sub-nanometer scales [4]. However, environmental factors such as mechanical vibration, electrical noise, and thermal fluctuations will inevitably generate noise in the STM data [50], fundamentally limiting its spatial resolution. While the noise reduction of STM data is generally challenging with conventional methods, it provides a meaningful real-world example to test the denoising capability of the proposed PDA-Net architecture.

### A. Physics-based Model to Generate Simulated STM Images

Our physical system of interest is (111) surface of copper single crystals, i.e., Cu(111), which hosts a Shockley-type surface state described by an effective Hamiltonian operator,

$$\hat{H}_0 = \frac{k^2}{2m_{\text{eff}}} - \mu. \quad (9)$$

Here,  $\mathbf{k} = (k_x, k_y)$  is the crystal momentum of surface electrons. The chemical potential for Cu(111) is  $\mu = 0.45$  eV, and  $m_{\text{eff}} = 0.38m_e$  is the effective mass of surface electrons, where  $m_e$  denotes the bare electron mass. When an atomically sharp STM tip approaches the surface of Cu(111), it injects an electron into Cu(111) through the quantum tunneling effect. The injected electron will propagate across the surface like a plain wave until it scatters with lattice impurities or defects. The scattered electron wave will superpose with the injected wave, forming an interference pattern and sending

a signal back to the STM probe. Moving the STM probe across the sample and performing measurements repeatedly will generate local density of states (LDOS) images that map out the electron density distribution of Cu(111) [51].

We exploit the Green's function method to simulate the above physical process [52]. Specifically, we use  $\hat{V}(\mathbf{r})$  to denote the potential function that describes  $N$  point-like impurities randomly distributed on the surface. The Hamiltonian of Cu(111) with defects will then be updated to  $\hat{H} = \hat{H}_0 + \hat{V}(\mathbf{r})$ , with the corresponding stationary Schrödinger equation as  $\hat{H}|\psi_\alpha(\mathbf{r})\rangle = E_\alpha|\psi_\alpha(\mathbf{r})\rangle$ . Here,  $|\psi_\alpha(\mathbf{r})\rangle$  is the electron eigenstate with an energy  $E_\alpha$ , where  $\alpha$  is a state index. Hence, the retarded Green's function of the system at a frequency  $\omega$  is defined as

$$\mathcal{G}(\mathbf{r}', \mathbf{r}, \omega) = \sum_{\alpha} \frac{\psi_{\alpha}^*(\mathbf{r})\psi_{\alpha}(\mathbf{r}')}{\omega - E_{\alpha} + i\eta}, \quad (10)$$

where  $\eta$  is an infinitesimal positive number. The LDOS function  $\mathcal{A}(\mathbf{r}, \omega)$  is then related to the Green's function via

$$\mathcal{A}(\mathbf{r}, \omega) = -\frac{1}{\pi} \text{Im} \mathcal{G}(\mathbf{r}', \mathbf{r}, \omega) \quad (11)$$

which is used to generate the simulated STM images.

### B. STM Setup to Generate Experimental STM Images

In the physical experiments, we prepared copper samples with atomically flat (111) surfaces, i.e., Cu(111), inside the ultra-high-vacuum (UHV) chamber using a sputtering-annealing cycles [53]. To acquire real-world experimental images, we used a low-temperature STM that operates at the pressure of  $< 10^{-10}$  torr and the base temperature of 4.2 K. The Cu(111) sample was scanned by the STM at a bias voltage of 10 mV and a current set point of 1 nA, which is the parameter setting optimized to achieve high-resolution imaging of the surface features. 50 experimental STM images were acquired to test the performance of our denoising model.

### C. Neural Network Architecture and Optimization

The generators  $G_{DA}$ ,  $G_D$ , and  $G_B$  share the same neural network architecture, as shown in Fig. 1. Specifically, the Down block consists of three convolutional layers. The first convolutional layer has a kernel size of  $7 \times 7$ , a stride of 1, a reflection padding of 3. The subsequent two convolutional layers have a kernel size of  $3 \times 3$ , a stride of 2, and a padding of 1. The ResNet block comprises nine residual connection blocks, each containing two convolutional layers with a kernel size of  $3 \times 3$ , a stride of 1, and reflection padding of 1. The Up block reconstructs the feature map back to the original image size. It mirrors the Down block, consisting of two deconvolutional layers with a kernel size of  $3 \times 3$ , a stride of 2, and a padding of 1, followed by a final convolutional layer with a kernel size of  $7 \times 7$ , a stride of 1, a reflection padding of 3. The discriminators  $D_D$ ,  $D_B$ , and  $D_{DA}$  adopt the PatchGAN discriminator architecture without modification [9]. The weighting hyperparameters that determine the contribution of different loss terms play a crucial role in training PDA-Net; we empirically set  $\lambda_D = \lambda_B = \lambda_{cyc} = \lambda_{DA} = 1$ , while  $\lambda_{FA} = 0.1$ . The PDA-Net is optimized using the Adam

optimizer with a default learning rate of 0.0002 for all network training. The momentum parameter is set to 0.5. Training is conducted on an NVIDIA A100 GPU with 80 GB memory, ensuring efficient computation and handling of large-scale datasets.

### D. Performance evaluation

During the training process, we prepared 3,600 images each for simulated clear images ( $I_S$ ) and simulated blurry images ( $I_{BS}$ ). The 61 experimental images are split into training and testing sets, with 50 images undergoing augmentation (flipping, rotating, and cropping) to create a training set of 3,600 images ( $I_E$ ). The remaining 11 images are augmented to generate 200 test images. For quantitative evaluation, the test set consists of 200 simulated blurry images ( $T_{BS}$ ) and 200 experimental images ( $T_E$ ) are passed through the trained generators  $G_D^*$  and  $G_{DA}^*$  for denoising.

We employed three full-reference quality metrics—*MSE*, *PSNR*, and *SSIM*—which compare denoised simulated blurry images in the test set  $T_{BS}^D$  to the original clear images. To quantify the quality of denoised experimental images from the test set ( $T_E^D$ ), we use two no-reference metrics—*PIQE* and *BRISQUE*—to assess the image naturalness. Their definitions are described below:

- *Mean Squared Error (MSE)*: *MSE* measures the average squared difference between corresponding pixels of two images, often used to quantify the difference between a reference image and a distorted image.

$$MSE = \frac{1}{mn} \sum_{i=1}^m \sum_{j=1}^n [T_{BS}^D(i, j) - T_S(i, j)]^2 \quad (12)$$

where  $m \times n$  is the image size,  $T_S$  is the clear simulated image, and  $T_{BS}^D$  is the denoised simulated image generated by our model, i.e.,  $T_{BS}^D = G_D^*(T_{BS})$ , where  $T_{BS}$  is simulated blurred image from  $T_S$  in test set.

- *Peak Signal-to-Noise Ratio (PSNR)*[54]: *PSNR* is defined as a ratio that compares the maximum possible pixel value of an image to the power of noise:

$$PSNR = 10 \log_{10} \left( \frac{255^2}{MSE} \right) \quad (13)$$

A higher PSNR value indicates better image quality, with less distortion relative to the reference image.

- *Structural Similarity Index (SSIM)*: While *MSE* and *PSNR* are widely used for image quality assessment, they have limitations in capturing perceptual differences as they primarily measure pixel-wise errors. As such, we employ *SSIM*, which offers a more perceptually accurate evaluation by considering luminance, contrast, and structural information [55]. It is mathematically defined as:

$$SSIM(T_{BS}^D, T_S) = \frac{(2\mu_D\mu_S + C_1)(2\sigma_{DS} + C_2)}{(\mu_D^2 + \mu_S^2 + C_1)(\sigma_D^2 + \sigma_S^2 + C_2)} \quad (14)$$

where  $\mu_D$  and  $\mu_S$  are the means of images of  $T_{BS}^D$  and  $T_S$ ,  $\sigma_D$  and  $\sigma_S$  are the corresponding variances,  $\sigma_{DS}$  is



the covariance, and  $C_1$  and  $C_2$  are constants to stabilized the division. SSIM values range from -1 to 1 with higher values indicating better image quality.

- *PIQE and BRISQUE*: *PIQE* (Perception-based Image Quality Evaluator) [56] and *BRISQUE* (Blind/Referenceless Image Spatial Quality Evaluator) [57] are image quality assessment models without needing a reference image. Both models utilize natural scene statistics to analyze the inherent image properties, capturing deviations from expected natural characteristics. *PIQE* focuses on detecting perceptually significant distortions based on a block-wise analysis, where it divides the image into smaller blocks and evaluates the quality of each block separately. In contrast, *BRISQUE* employs a regression model, typically a support vector machine (SVM), to predict quality scores from spatial domain features. For both metrics, lower scores indicate better image quality.

#### E. Results for deblurring the simulated blurry images

The goal of the current investigation is to denoise the simulated blurry STM images shown in Fig. 3(b), and compare them with the original simulated clear images presented in Fig. 3(a). We conduct an ablation study to assess the impact of each module designed in our PDA-Net on the deblurring performance in the simulation domain. The denoising performance is benchmarked with the results produced by the sole cycle-consistency (i.e., CycleGAN) model without domain adaptation, weight sharing, or feature alignment. We present both quantitative and qualitative results for three variants of our methodology, with each variant incorporating additional components progressively: (1) cycle-consistency module enhanced with domain adversarial (DA) module (i.e., CycleGAN+DA), (2) cycle-consistency and DA module with shared weights (i.e., CycleGAN+DA+WS), and (3) cycle-consistency and DA module with both shared weights and feature alignment (i.e., PDA-Net).

The *MSE*, *PSNR*, and *SSIM* for each variant and original CycleGAN model are presented in Table I. The visual comparisons are shown in Fig. 3(d,e,f), respectively. According to Table I, CycleGAN generates a high *MSE* and relatively low *PSNR* with a high *SSIM*, along with the good deblurring results visualized in Fig. 3(c). This indicates that while the pixel-wise error (*MSE*) and signal-to-noise ratio (*PSNR*) suggest room for improvement, the structural similarity (*SSIM*) and visual inspection confirm that the sole CycleGAN model can effectively preserve image details and structures when sufficient unpaired training data are provided. After adding the domain adversarial module (i.e., CycleGAN+DA), there is a notable reduction in *MSE* and an increase in *PSNR*, albeit with a slight drop in *SSIM*. Incorporating weight sharing (i.e., CycleGAN+DA+WS) further improves *MSE* and *PSNR* while maintaining a high *SSIM*. Finally, the proposed PDA-Net model, which includes feature alignment, yields the best overall performance with the lowest *MSE* of 513.06, highest *PSNR* of 25.54, and highest *SSIM* of 0.9332.

Compared with a pure CycleGAN, our PDA-Net achieves an improvement of 58.74% on *MSE*, 10.37% on *PSNR*, and

TABLE I: The ablation study on denoising simulated blurry images.

	<i>MSE</i>	<i>PSNR</i>	<i>SSIM</i>
CycleGAN	1243.33	23.14	0.9002
CycleGAN+DA	1144.40	23.43	0.8840
CycleGAN+DA+WS	822.54	24.65	0.8938
PDA-Net	513.06	25.54	0.9332

Note: DA refers to Domain Adversarial module, WS refers to Weight Sharing, and the proposed PDA-Net further includes feature alignment.

TABLE II: The ablation study on denoising real-world experimental images.

	<i>BRISQUE</i>	<i>PIQE</i>
Experimental Images ( $T_E$ )	69.96	96.15
CycleGAN	114.40	59.14
CycleGAN+DA	78.93	70.11
CycleGAN+DA+WS	69.80	71.77
PDA-Net	52.99	56.80

3.67% on *SSIM*, demonstrating a comprehensive enhancement in both pixel-wise accuracy and structural similarity. The performance enhancement is due to the novel design of our PDA-Net. Specifically, domain adaptation allows the PDA-Net to better generalize across both simulated and real experimental domains, improving overall denoising performance. Weight sharing not only improve the training efficiency but also retains beneficial features learned from both generators (i.e.,  $G_D$  and  $G_{DA}$ ), enabling effective knowledge sharing across both domains. Feature alignment ensures that the lower-level features extracted from both generators are harmonized, leading to a more robust and coherent representation of the image data across both domains.

#### F. Results for deblurring the real-world experimental images

Obtaining noise-free STM images is impractical due to environmental and equipment limitations. This limitation poses a significant challenge for existing denoising models, as they often rely on access to clear reference images for training and evaluation. Moreover, collecting a sufficient number of experimental STM images for unsupervised denoising is costly and time-consuming. Given these constraints, existing methods struggle to generalize effectively to real-world STM data. In this experimental study, we evaluate the proposed PDA-Net, which, to the best of our knowledge, is the first model specifically designed to operate under these constraints. As no directly comparable works exist in the literature, we benchmark our denoising results on experimental images against a CycleGAN model pretrained on the simulated dataset. Additionally, an ablation study is conducted to assess the effectiveness of key components, including domain adaptation, weight sharing, and feature alignment modules.

Fig. 4 provides visual examples of the denoising results in the real experimental domain. Fig. 4(a) shows the experimental STM images of the Cu atom. Fig. 4(c) presents the



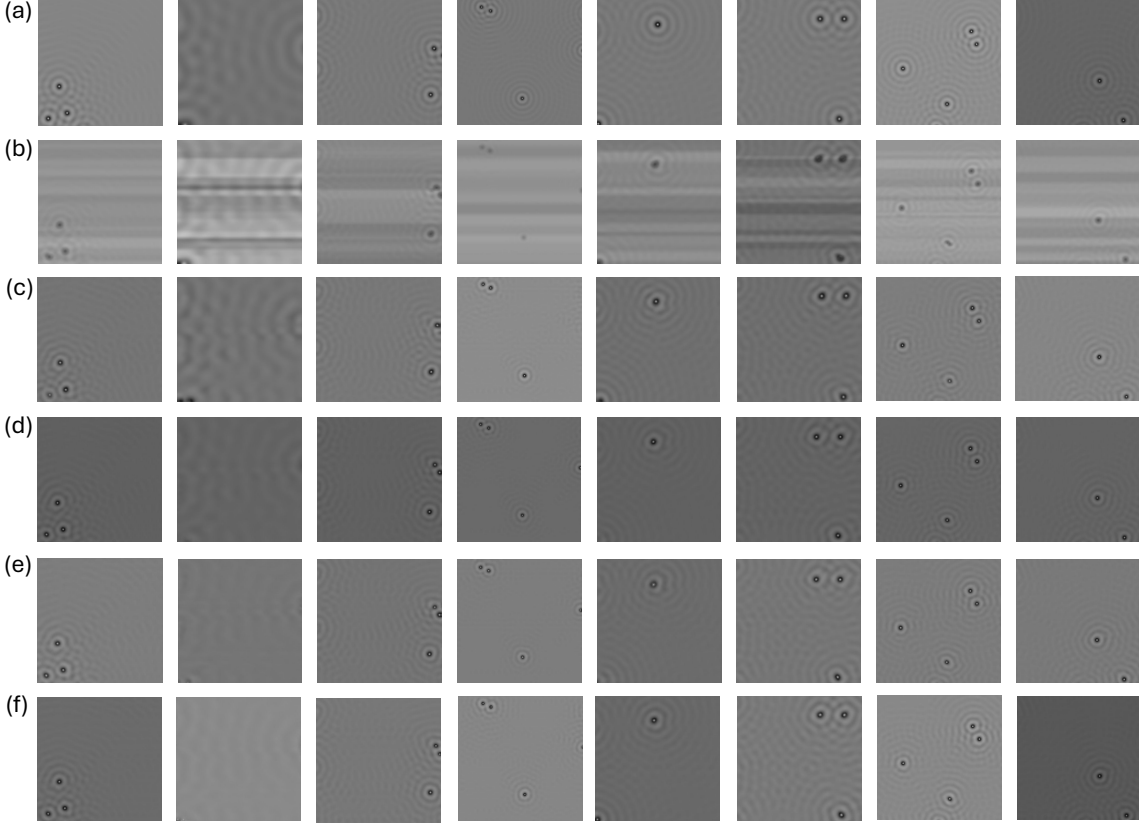


Fig. 3: Examples of (a) The simulated clear images ( $I_S$ ); (b) The simulated blurry images ( $I_{BS}$ ); (c) image deblurred from  $I_{BS}$  using pure CycleGAN model; (d) images deblurred from  $I_{BS}$  using CycleGAN with domain adversarial (DA) module; (e) images deblurred from  $I_{BS}$  using CycleGAN and DA with weight sharing; (f) images deblurred from  $I_{BS}$  using the proposed PDA-Net model, i.e.,  $I_{BS}^D$ .

denoising results from CycleGAN+DA, where noise reduction is achieved for most experimental images. However, some disadvantages still appear. For example, the last image in Fig. 4(c) does not deblur to the expected denoised pattern. The absence of a central hollow/white dot in the middle of the atom indicates a non-ideal restoration of the atomic structure, and the electron wave pattern fails to appear as expected. Fig. 4(d) depicts the results generated by CycleGAN+DA+WS, which display improved image clarity. Specifically, the details of the images, such as the wave pattern, start to become more clear, as seen in the third image in Fig. 4(d). The center of the Cu atom also becomes clear as shown in the last image of Fig. 4(d). However, the electron pattern is still not completely watched by the model. Fig. 4(e) demonstrates the performance of the proposed PDA-Net. The wave patterns are fully captured by the model for all images, and the centers of Cu atoms are clearly presented. The proposed PDA-Net delivers the best denoising results with minimal artifacts and clear details. In contrast, Fig. 4(b) presents the deblurring results of experimental images using the pretrained CycleGAN model learned exclusively on the simulated dataset, without the DA module or WS and feature alignment techniques, which displays significant distortion compared to any variant of our PDA-Net.

Table 2 presents the quantitative results on real-world ex-

perimental STM images, evaluated using the *BRISQUE* and *PIQE*. The baseline experimental images have a *BRISQUE* score of 69.96 and a *PIQE* score of 96.15. The CycleGAN model shows a degradation in perceived quality with a *BRISQUE* score of 114.40, while the *PIQE* score improves to 59.14. Adding the DA module (CycleGAN+DA) significantly reduces the *BRISQUE* score to 78.93 but slightly increases the *PIQE* score to 70.11. Incorporating WS (CycleGAN+DA+WS) further enhances the results, achieving a *BRISQUE* score of 69.80 and a *PIQE* score of 71.77. The proposed PDA-Net model, which further includes feature alignment, achieves the best results with a *BRISQUE* score of 52.99 and a *PIQE* score of 56.80, demonstrating superior image quality as perceived by both metrics.

## V. CONCLUSIONS

In this paper, we develop a novel framework, PDA-Net, for real-world STM image denoising. We first leverage physics principles to generate simulated clear/blurry STM images, which serves as the foundation to construct the denoising model for real-world experimental image denoising. Second, we incorporate a cycle-consistency module to ensure the reliability of the denoising process in the simulation domain. Innovatively, we introduce a domain adversarial module to guide the domain adaptation generator in producing denoised

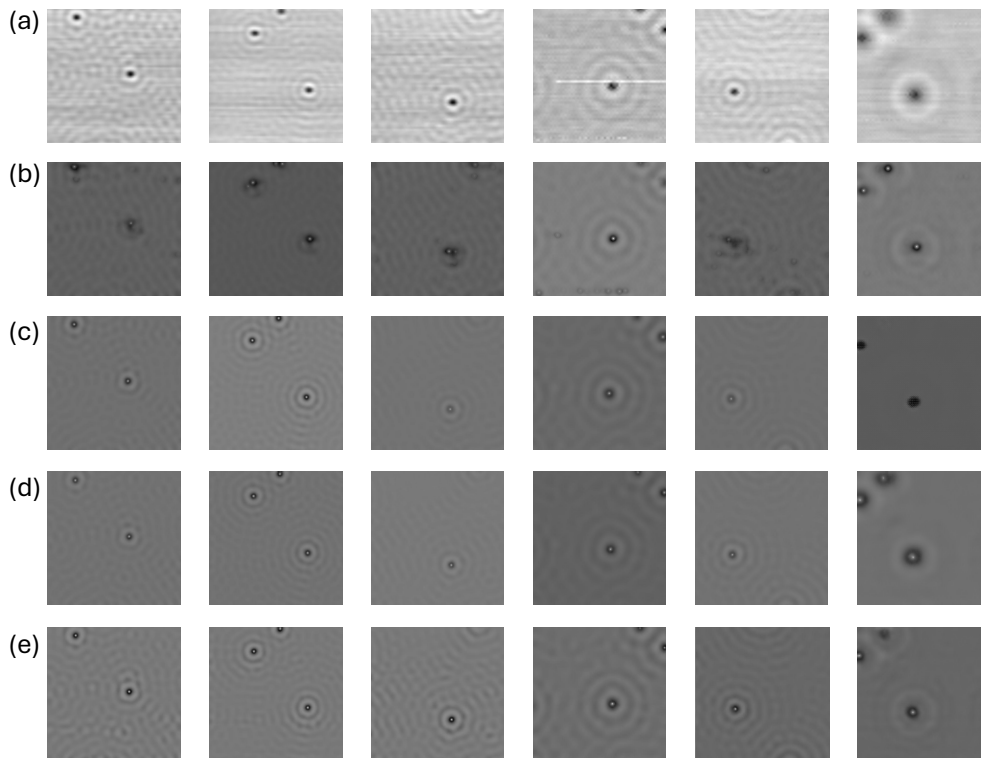


Fig. 4: Examples of (a) Experimental images  $I_E$ ; (b) images deblurred from  $I_E$  using the pretrained CycleGAN model without domain adversarial (DA) module. (c) images deblurred from  $I_E$  using CycleGAN and DA module; (d) images deblurred from  $I_E$  using CycleGAN and DA with weight sharing; (e) images deblurred from  $I_E$  using the proposed PDA-Net model, i.e.,  $I_E^D$ .

STM images in the real experimental domain that are similar to the simulated clear benchmark. Moreover, feature alignment and weight sharing are engaged to further enable knowledge transfer from the simulated domain to the real-world denoising domain adaptation generator, thereby improving the performance of real-world denoising tasks. PDA-Net overcomes the limitations of traditional unsupervised denoising methods that typically require a set of clear images for training. Finally, we evaluate the proposed PDA-Net on both simulated and real-world STM datasets, with experimental results confirming its effectiveness in enhancing image quality. The PDA-Net framework not only facilitates more accurate analysis and interpretation in quantum material research but also has the potential for application in other complex imaging scenarios, such as medical image denoising.

## VI. ACKNOWLEDGEMENT

This research has been partially supported by a seed grant from the AI Tennessee Initiative at the University of Tennessee Knoxville. This research was partially supported by the National Science Foundation Materials Research Science and Engineering Center program through the UT Knoxville Center for Advanced Materials and Manufacturing (DMR-2309083). Author Jianxin Xie acknowledges the start-up funding support from the University of Virginia, School of Data Science. Author Bing Yao also acknowledges the funding support from the National Heart, Lung, And Blood Institute of the National Institutes of Health under Award Number R01HL172292.

## REFERENCES

- [1] G. B. Frisoni, N. C. Fox, C. R. Jack Jr, P. Scheltens, and P. M. Thompson, "The clinical use of structural mri in alzheimer disease," *Nature reviews neurology*, vol. 6, no. 2, pp. 67–77, 2010.
- [2] B. K. Rutt and D. H. Lee, "The impact of field strength on image quality in mri," *Journal of Magnetic Resonance Imaging*, vol. 6, no. 1, pp. 57–62, 1996.
- [3] J. Xie and B. Yao, "Hierarchical active learning for defect localization in 3d systems," *IIEE Transactions on Healthcare Systems Engineering*, vol. 14, no. 2, pp. 115–129, 2024.
- [4] G. Binnig and H. Rohrer, "Scanning tunneling microscopy—from birth to adolescence," *Reviews of Modern Physics*, vol. 59, no. 3, p. 615, 1987.
- [5] W. A. Hofer, A. S. Foster, and A. L. Shluger, "Theories of scanning probe microscopes at the atomic scale," *Reviews of Modern Physics*, vol. 75, no. 4, p. 1287, 2003.
- [6] Y. LeCun, L. Bottou, Y. Bengio, and P. Haffner, "Gradient-based learning applied to document recognition," *Proceedings of the IEEE*, vol. 86, no. 11, pp. 2278–2324, 1998.
- [7] J.-Y. Zhu, T. Park, P. Isola, and A. A. Efros, "Unpaired image-to-image translation using cycle-consistent adversarial networks," in *Proceedings of the IEEE international conference on computer vision*, 2017, pp. 2223–2232.
- [8] Z. Yi, H. Zhang, P. Tan, and M. Gong, "Dualgan: Unsupervised dual learning for image-to-image translation," in *Proceedings of the IEEE international conference on computer vision*, 2017, pp. 2849–2857.
- [9] P. Isola, J.-Y. Zhu, T. Zhou, and A. A. Efros, "Image-to-image translation with conditional adversarial networks," in *Proceedings of the IEEE conference on computer vision and pattern recognition*, 2017, pp. 1125–1134.
- [10] M.-Y. Liu, T. Breuel, and J. Kautz, "Unsupervised image-to-image translation networks," *Advances in neural information processing systems*, vol. 30, 2017.
- [11] P. Rerkkumsup, M. Aketagawa, K. Takada, Y. Togawa, N. T. Thinh, and Y. Kozuma, "Highly stable atom-tracking scanning tunneling microscopy," *Review of Scientific Instruments*, vol. 75, no. 4, pp. 1061–1067, 2004.

- [12] L. Fan, F. Zhang, H. Fan, and C. Zhang, "Brief review of image denoising techniques," *Visual Computing for Industry, Biomedicine, and Art*, vol. 2, no. 1, p. 7, 2019.
- [13] B. S. Kumar, "Image denoising based on gaussian/bilateral filter and its method noise thresholding," *Signal Image Video Process.*, vol. 7, no. 6, pp. 1159–1172, 2013.
- [14] S. Shrestha, "Image denoising using new adaptive based median filters," *arXiv preprint arXiv:1410.2175*, 2014.
- [15] B. Ergen, *Signal and image denoising using wavelet transform*. InTech London, UK, 2012.
- [16] C. Tian, M. Zheng, W. Zuo, B. Zhang, Y. Zhang, and D. Zhang, "Multi-stage image denoising with the wavelet transform," *Pattern Recognition*, vol. 134, p. 109050, 2023.
- [17] N. You, L. Han, D. Zhu, and W. Song, "Research on image denoising in edge detection based on wavelet transform," *Applied Sciences*, vol. 13, no. 3, p. 1837, 2023.
- [18] J. Xie, S. Stavrakakis, and B. Yao, "Automated identification of atrial fibrillation from single-lead ecgs using multi-branching resnet," *Frontiers in Physiology*, vol. 15, p. 1362185, 2024.
- [19] Z. Wang, S. Stavrakakis, and B. Yao, "Hierarchical deep learning with generative adversarial network for automatic cardiac diagnosis from ecg signals," *Computers in Biology and Medicine*, vol. 155, p. 106641, 2023.
- [20] K. Zhang, W. Ren, W. Luo, W.-S. Lai, B. Stenger, M.-H. Yang, and H. Li, "Deep image deblurring: A survey," *International Journal of Computer Vision*, vol. 130, no. 9, pp. 2103–2130, 2022.
- [21] C. Min, G. Wen, B. Li, and F. Fan, "Blind deblurring via a novel recursive deep cnn improved by wavelet transform," *IEEE Access*, vol. 6, pp. 69 242–69 252, 2018.
- [22] L. Huang and Y. Xia, "Joint blur kernel estimation and cnn for blind image restoration," *Neurocomputing*, vol. 396, pp. 324–345, 2020.
- [23] Z. Shen, W.-S. Lai, T. Xu, J. Kautz, and M.-H. Yang, "Deep semantic face deblurring," in *Proceedings of the IEEE conference on computer vision and pattern recognition*, 2018, pp. 8260–8269.
- [24] J. Johnson, A. Alahi, and L. Fei-Fei, "Perceptual losses for real-time style transfer and super-resolution," in *Computer Vision—ECCV 2016: 14th European Conference, Amsterdam, The Netherlands, October 11–14, 2016, Proceedings, Part II 14*. Springer, 2016, pp. 694–711.
- [25] B. Lu, J.-C. Chen, and R. Chellappa, "Uid-gan: Unsupervised image deblurring via disentangled representations," *IEEE Transactions on Biometrics, Behavior, and Identity Science*, vol. 2, no. 1, pp. 26–39, 2019.
- [26] K. Zhang, W. Luo, Y. Zhong, L. Ma, B. Stenger, W. Liu, and H. Li, "Deblurring by realistic blurring," in *Proceedings of the IEEE/CVF conference on computer vision and pattern recognition*, 2020, pp. 2737–2746.
- [27] A. Vaswani, N. Shazeer, N. Parmar, J. Uszkoreit, L. Jones, A. N. Gomez, L. Kaiser, and I. Polosukhin, "Attention is all you need," *Advances in neural information processing systems*, vol. 30, 2017.
- [28] D. Zhang, Z. Liang, and J. Shao, "Joint image deblurring and super-resolution with attention dual supervised network," *Neurocomputing*, vol. 412, pp. 187–196, 2020.
- [29] S. Nah, T. Hyun Kim, and K. Mu Lee, "Deep multi-scale convolutional neural network for dynamic scene deblurring," in *Proceedings of the IEEE conference on computer vision and pattern recognition*, 2017, pp. 3883–3891.
- [30] K. Kim, S. Lee, and S. Cho, "Mssnet: Multi-scale-stage network for single image deblurring," in *European conference on computer vision*. Springer, 2022, pp. 524–539.
- [31] J. Dong, J. Pan, Z. Yang, and J. Tang, "Multi-scale residual low-pass filter network for image deblurring," in *Proceedings of the IEEE/CVF International Conference on Computer Vision*, 2023, pp. 12 345–12 354.
- [32] C.-M. Fan, T.-J. Liu, and K.-H. Liu, "Sunet: Swin transformer unet for image denoising," in *2022 IEEE International Symposium on Circuits and Systems (ISCAS)*. IEEE, 2022, pp. 2333–2337.
- [33] K. Yi, Y. Ge, X. Li, S. Yang, D. Li, J. Wu, Y. Shan, and X. Qie, "Masked image modeling with denoising contrast," *arXiv preprint arXiv:2205.09616*, 2022.
- [34] F.-J. Tsai, Y.-T. Peng, Y.-Y. Lin, C.-C. Tsai, and C.-W. Lin, "Stripformer: Strip transformer for fast image deblurring," in *European conference on computer vision*. Springer, 2022, pp. 146–162.
- [35] I. Goodfellow, J. Pouget-Abadie, M. Mirza, B. Xu, D. Warde-Farley, S. Ozair, A. Courville, and Y. Bengio, "Generative adversarial nets," *Advances in neural information processing systems*, vol. 27, 2014.
- [36] S. Zhao, Z. Zhang, R. Hong, M. Xu, Y. Yang, and M. Wang, "Fcl-gan: A lightweight and real-time baseline for unsupervised blind image deblurring," in *Proceedings of the 30th ACM International Conference on Multimedia*, 2022, pp. 6220–6229.
- [37] T. Kwon and J. C. Ye, "Cycle-free cyclegan using invertible generator for unsupervised low-dose ct denoising," *IEEE Transactions on Computational Imaging*, vol. 7, pp. 1354–1368, 2021.
- [38] K. Zhang, T. Niu, and L. Xu, "Decogan: Mvct image denoising via coupled generative adversarial network," *Physics in Medicine & Biology*, vol. 69, no. 14, p. 145007, 2024.
- [39] H. S. Park, J. Baek, S. K. You, J. K. Choi, and J. K. Seo, "Unpaired image denoising using a generative adversarial network in x-ray ct," *IEEE Access*, vol. 7, pp. 110414–110425, 2019.
- [40] Y. Ganin and V. Lempitsky, "Unsupervised domain adaptation by back-propagation," in *International conference on machine learning*. PMLR, 2015, pp. 1180–1189.
- [41] M.-Y. Liu and O. Tuzel, "Coupled generative adversarial networks," *Advances in neural information processing systems*, vol. 29, 2016.
- [42] E. Tzeng, J. Hoffman, K. Saenko, and T. Darrell, "Adversarial discriminative domain adaptation," in *Proceedings of the IEEE conference on computer vision and pattern recognition*, 2017, pp. 7167–7176.
- [43] J. Hoffman, E. Tzeng, T. Park, J.-Y. Zhu, P. Isola, K. Saenko, A. Efros, and T. Darrell, "Cycada: Cycle-consistent adversarial domain adaptation," in *International conference on machine learning*. Pmlr, 2018, pp. 1989–1998.
- [44] S. Lee, S. Cho, and S. Im, "Dranet: Disentangling representation and adaptation networks for unsupervised cross-domain adaptation," in *Proceedings of the IEEE/CVF conference on computer vision and pattern recognition*, 2021, pp. 15 252–15 261.
- [45] K. Lin, T. H. Li, S. Liu, and G. Li, "Real photographs denoising with noise domain adaptation and attentive generative adversarial network," in *Proceedings of the IEEE/CVF conference on computer vision and pattern recognition workshops*, 2019, pp. 0–0.
- [46] M. Li, J. Wang, Y. Chen, Y. Tang, Z. Wu, Y. Qi, H. Jiang, J. Zheng, and B. M. Tsui, "Low-dose ct image synthesis for domain adaptation imaging using a generative adversarial network with noise encoding transfer learning," *IEEE transactions on medical imaging*, vol. 42, no. 9, pp. 2616–2630, 2023.
- [47] S. Deng, Y. Chen, W. Huang, R. Zhang, and Z. Xiong, "Unsupervised domain adaptation for em image denoising with invertible networks," *IEEE Transactions on Medical Imaging*, 2024.
- [48] W. Li and J. Wang, "Residual learning of cycle-gan for seismic data denoising," *IEEE access*, vol. 9, pp. 11 585–11 597, 2021.
- [49] J. Gu and J. C. Ye, "Adain-based tunable cyclegan for efficient unsupervised low-dose ct denoising," *IEEE Transactions on Computational Imaging*, vol. 7, pp. 73–85, 2021.
- [50] X. Wang, X. Lin, V. Dravid, J. Ketterson, and R. Chang, "Stable glow discharge for synthesis of carbon nanotubes," *Applied Physics Letters*, vol. 66, no. 4, pp. 427–429, 1995.
- [51] M. Crommie, C. P. Lutz, and D. Eigler, "Imaging standing waves in a two-dimensional electron gas," *Nature*, vol. 363, no. 6429, pp. 524–527, 1993.
- [52] G. A. Fiete and E. J. Heller, "Colloquium: Theory of quantum corrals and quantum mirages," *Reviews of Modern Physics*, vol. 75, no. 3, p. 933, 2003.
- [53] L. Marks, R. Ai, J. Bonevich, M. Buckett, D. Dunn, J. Zhang, M. Jacoby, and P. Stair, "UHV microscopy of surfaces," *Ultramicroscopy*, vol. 37, no. 1–4, pp. 90–102, 1991.
- [54] J. Zhang, G. Lin, L. Wu, C. Wang, and Y. Cheng, "Wavelet and fast bilateral filter based de-speckling method for medical ultrasound images," *Biomedical Signal Processing and Control*, vol. 18, pp. 1–10, 2015.
- [55] Z. Wang, A. C. Bovik, H. R. Sheikh, and E. P. Simoncelli, "Image quality assessment: from error visibility to structural similarity," *IEEE transactions on image processing*, vol. 13, no. 4, pp. 600–612, 2004.
- [56] N. Venkatanath, D. Praneeth, M. C. Bh, S. S. Channappayya, and S. S. Medasani, "Blind image quality evaluation using perception based features," in *2015 twenty first national conference on communications (NCC)*. IEEE, 2015, pp. 1–6.
- [57] A. Mittal, A. K. Moorthy, and A. C. Bovik, "No-reference image quality assessment in the spatial domain," *IEEE Transactions on image processing*, vol. 21, no. 12, pp. 4695–4708, 2012.